Gain-of-function *MYCN* causes a megalencephaly-polydactyly syndrome manifesting mirror phenotypes of Feingold syndrome

Yosuke Nishio,[1,2,3,13] Kohji Kato,[1,2,3,13,*] Frederic Tran Mau-Them,[4,5] Hiroshi Futagawa,[6] Chloé Quélin,[7] Saori Masuda,[8] Antonio Vitobello,[4,5] Shiomi Otsuji,[1] Hossam H. Shawki,[9] Hisashi Oishi,[9] Christel Thauvin-Robinet,[4,5,10] Toshiki Takenouchi,[11] Kenjiro Kosaki,[12] Yoshiyuki Takahashi,[2] and Shinji Saitoh[1,14,*]

Summary

MYCN, a member of the MYC proto-oncogene family, regulates cell growth and proliferation. Somatic mutations of *MYCN* are identified in various tumors, and germline loss-of-function variants are responsible for Feingold syndrome, characterized by microcephaly. In contrast, one megalencephalic patient with a gain-of-function variant in *MYCN*, p.Thr58Met, has been reported, and additional patients and pathophysiological analysis are required to establish the disease entity. Herein, we report two unrelated megalencephalic patients with polydactyly harboring *MYCN* variants of p.Pro60Leu and Thr58Met, along with the analysis of gain-of-function and loss-of-function Mycn mouse models. Functional analyses for MYCN-Pro60Leu and MYCN-Thr58Met revealed decreased phosphorylation at Thr58, which reduced protein degradation mediated by FBXW7 ubiquitin ligase. The gain-of-function mouse model recapitulated the human phenotypes of megalencephaly and polydactyly, while brain analyses revealed excess proliferation of intermediate neural precursors during neurogenesis, which we determined to be the pathomechanism underlying megalencephaly. Interestingly, the kidney and female reproductive tract exhibited overt morphological anomalies, possibly as a result of excess proliferation during organogenesis. In conclusion, we confirm an MYCN gain-of-function-induced megalencephaly-polydactyly syndrome, which shows a mirror phenotype of Feingold syndrome, and reveal that MYCN plays a crucial proliferative role, not only in the context of tumorigenesis, but also organogenesis.

Introduction

MYCN (MIM: 164840) is a member of the MYC proto-oncogene family composed of *MYC* (MIM: 190080), *MYCL* (MIM: 164850) and *MYCN*.[1] MYC proteins act as transcription factors that regulate the expression of various genes involved in fundamental cellular processes, such as cell proliferation, differentiation, and apoptosis,[2,3] although emerging evidence also suggests target gene-independent functions, such as the promotion of transcription termination and transcription elongation.[4] *MYCN* was identified as a proto-oncogene amplified in neuroblastoma, which is found in 20%–30% of neuroblastoma patients and considered to be one of the poorest prognostic markers.[5] In addition, *MYCN* amplification is also detected in other cancers, including Wilms' tumor, rhabdomyosarcomas, and lung cancers.[6]

MYCN and other MYC proteins are expressed, not only in tumors, but also in the developing human fetal brain, limbs, heart, kidney, and lung tissues.[7–10] Unsurprisingly, based on these expression patterns, heterozygote loss-of-function *MYCN* variants adversely affect fetal development, causing a genetic syndrome with congenital multiple anomalies, called Feingold syndrome (MIM: 164280). Characteristic features of Feingold syndrome consist of microcephaly, intellectual disability, esophageal and duodenal atresia, and limb malformation, such as absent/hypoplastic phalanx.[11,12] In a loss-of-function mouse model, germline homozygous mice were embryonic lethal and manifested histological abnormalities of the central nervous system, mesonephros, and lung, indicating essential functions for MYCN during fetal development.[13] Furthermore, neural crest-specific *Mycn* conditional knock-out mice exhibit decreased proliferation of granule neuron progenitors in the cerebellum, leading to decreased foliation and reduced cerebellar mass.[14] Aside from the central nervous system, skeletal mesenchymal stem cell-specific *Mycn* conditional

[1]Department of Pediatrics and Neonatology, Nagoya City University Graduate School of Medical Sciences, Nagoya 467-8601, Japan; [2]Department of Pediatrics, Nagoya University Graduate School of Medicine, Nagoya 466-8560, Japan; [3]Department of Genetics, Research Institute of Environmental Medicine, Nagoya University, Nagoya 464-8601, Japan; [4]Unité Fonctionnelle 6254 d'Innovation en Diagnostique Génomique des Maladies Rares, Pôle de Biologie, CHU Dijon Bourgogne, 21070 Dijon, France; [5]INSERM UMR1231 GAD, 21000 Dijon, France; [6]Department of Clinical Genetics, Tokyo Metropolitan Children's Medical Center, Tokyo 183-8561, Japan; [7]Service de Génétique Clinique, CLAD Ouest, CHU Rennes, Hôpital Sud, 35200 Rennes, France; [8]Department of Hematology and Oncology, Tokyo Metropolitan Children's Medical Center, Tokyo 183-8561, Japan; [9]Department of Comparative and Experimental Medicine, Nagoya City University Graduate School of Medical Sciences and Medical School, Nagoya 467-8601, Japan; [10]Centre de Référence Maladies Rares "Anomalies du développement et syndromes malformatifs", Centre de Génétique, FHU TRANSLAD et Institut GIMI, CHU Dijon Bourgogne, 21070 Dijon, France; [11]Department of Pediatrics, Keio University School of Medicine, Tokyo 160-8582, Japan; [12]Center for Medical Genetics, Keio University School of Medicine, Tokyo 160-8582, Japan
[13]These authors contributed equally
[14]Lead contact
*Correspondence: kohji.kato@bristol.ac.uk (K.K.), ss11@med.nagoya-cu.ac.jp (S.S.)
https://doi.org/10.1016/j.xhgg.2023.100238

knock-out mice recapitulate the limb abnormalities of Feingold syndrome, where down-regulation of the PI3K pathway has been suggested to be a partial pathophysiological cause of the skeletal defects.[15]

We previously reported a 15-year-old boy with a *de novo* gain-of-function *MYCN* variant (p.Thr58Met).[16] Interestingly, the variant is often identified as a somatic mutation in malignant tumors, such as neuroblastoma, astrocytoma, and mesonephric carcinoma.[17,18] Furthermore, glycogen synthase kinase 3 beta (MIM: 605004)-mediated phosphorylation at Thr58 (T58) destabilizes MYCN protein,[19,20] and functional analysis of T58M variants demonstrated decreased phosphorylation at T58, which resulted in accumulation of MYCN-T58M compared with wildtype (WT) because of reduced ubiquitination-mediated degradation.[16] This increased stability makes it possible for MYCN-T58M to up-regulate downstream targets *in vitro*. In contrast with the microcephaly and hypoplastic phalanx characterized in Feingold syndrome, the clinical phenotype of the gain-of-function MYCN-related disorder include megalencephaly, ventriculomegaly, postaxial polydactyly, and, notably, neuroblastoma during infancy.[16] The phenotypes partially overlap with those of megalencephaly-polymicrogyria-polydactyly-hydrocephalus syndrome 3 (MPPH3 [MIM: 615938]) caused by gain-of-function cyclin D2 (*CCND2* [MIM: 123833]) variants. Given that *CCND2* is one of the target genes of MYCN, it is not surprising that patients with the two disease conditions show similar clinical manifestations, although there are some distinct features, including morphological features of the corpus callosum and the presence or absence of polymicrogyria and hydrocephalus. However, our knowledge of the clinical details of *MYCN* gain-of-function-related disorders is limited because there have not been any additional patients reported to date. Furthermore, pathophysiological analyses of *MYCN* gain-of-function mutations have not been performed to date. Although many investigations relating to MYCN have been performed in both cellular and animal models, the investigations mainly targeted pathogenicity in malignant tumors or loss-of-function mutations in development.[13–15,21]

In this study, we present detailed clinical information of two patients with *de novo MYCN* variants, MYCN-Thr58Met and MYCN-Pro60Leu, which were identified through exome sequencing and whose gain-of-function nature was confirmed by cellular analysis. Both patients, a fetus subjected to termination of pregnancy and an 8-month-old boy, exhibited overlapping phenotypes with those observed in the previous case, including megalencephaly, ventriculomegaly, and postaxial polydactyly. Notably, the latter case developed neuroblastoma, as did our previous case. Furthermore, we established *MYCN* T58M knock-in mice as a gain-of-function model and investigated how MYCN contributes to normal embryonic development and how gain-of-function *MYCN* variants cause the characteristic symptoms in our patients. T58M knock-in mice recapitulated the patients' phenotypes, which was attributed to over-proliferation of tissues in the developing brain, kidney, and female reproductive system. Thus, gain-of-function *MYCN* variants cause a megalencephaly-polydactyly syndrome. In addition, cellular and pathological analyses of gain-of-function mouse models demonstrated important roles for Mycn during early development, which contributes to our understanding of organogenesis.

Material and methods

Animals

Mycn T58M/WT and FS/WT mice were generated with the CRISPR/Cas9-mediated gene editing system. Briefly, zygotes were injected with sgRNA and Cas9 protein, synthesized with PCR using the indicated primer (px-330-guide-forward: 5′-caccGCTGGGCGACAACGGGGGCGT-3′ and px-330-guide-reverse: 5′-aaacACGCCCCCGTTGTCGCCCAGC-3′), as well as a single-stranded oligodeoxynucleotide (5′-GGCGGTCCCGACTCGACCCCACCGGGGAGGACATCTGGAAGAAGTTTGAGCTGCTGCCCATGCCCCCCGGTTGTCGCCCAGCCGCGCCTTCCCAGAGCACAGCCCGGAGCCTTCGAATTGGG-3′), and then transferred to pseudo-pregnant female mice. The acquired F0 mice were crossed to C57BL/6NCr, purchased from Japan SLC, Inc., generating the F1 mice of each strain. Genotypes were validated with Sanger sequencing using the following primers: *Mycn* (forward: 5′-TGGTTGTAGAGTTGGAGG-3′; reverse: 5′-CGTGCTGTAGTTTTTCGT-3′). The mutant mice were backcrossed to a C57BL/6NCr background. Because mutant mice were unable to reproduce naturally, analyses were performed in mice born from embryos transplanted into ICR mice, purchased from Japan SLC, Inc. Desired mice were obtained by fertilizing WT oocytes with heterozygous sperm of the T58M/WT or FS/WT mice. All animals were group housed in an environment with temperatures ranging from 20°C to 26°C and humidity levels of 40%–60%, with a 12-h light and dark cycle. All animal experiments were approved by the Institutional Animal Experiment Committee of the Nagoya City University in accordance with all appropriate regulations and guidelines.

Whole-exome analysis

Genetic diagnosis was performed using whole-exome sequencing as described previously.[22,23] Briefly, genomic DNA was extracted from peripheral blood, partitioned using the SureSelect XT Human All Exon V6 capture library (Agilent Technologies) or Twist Comprehensive Exome Panel (Twist Bioscience), and DNA sequencing performed with a HiSeq 4000 or NovaSeq 6000 (Illumina) sequencer. After alignment to the reference genome (hg19), we excluded variants with a minor allele frequency over 0.5% in public databases, except previously identified pathogenic variants in the ClinVar database and the Human Gene Mutation Database. We then focused on nonsynonymous single nucleotide variants, insertions and deletions, and splice site variants. Identified variants were confirmed by Sanger sequencing of PCR-amplified products with the following primers: *MYCN* (forward: 5′-TACCCGGACGAAGATGAC-3′; reverse: 5′-CCCACAGCTCGTTCTCAA-3′).

Plasmids

pcDNA3-hemagglutinin-tagged human MYCN was obtained from Addgene (plasmid #71463). Site-directed mutagenesis (KOD-Plus

Mutagenesis Kit, Toyobo) was then used to generate MYCN-T58M and MYCN-P60L mutant constructs. Mouse Fbw7 cDNA, a kind gift from Prof. K. Nakayama (Kyushu University), was cloned into the pCAG-Myc vector. All constructs were verified by DNA sequencing.

Cell culture
HEK293T cells were cultured in DMEM (Gibco) supplemented with 10% FBS (Gibco), L-glutamine and penicillin-streptomycin (Sigma Aldrich). Transfection was performed with Lipofectamine 3000 (Thermo Fisher Scientific) according to the manufacturer's guidelines.

Protein extraction
Brains at various developmental stages were homogenized with 10 volumes of RIPA buffer (FUJIFILM, Wako Pure Chemical Corp) supplemented with protease inhibitor (Sigma-Aldrich) and incubated on ice. After incubation, the homogenate was sonicated with an ultrasonic homogenizer (Microtec Co., LTD.) and centrifuged at 15,000 rpm for 20 min. The supernatant was collected for further applications. Before analyses, protein concentrations were measured with a micro bicinchoninic acid protein assay kit (Pierce, Thermo Fisher Scientific) with bovine serum albumin as a standard.

Western blotting
Indicated amounts of tissue or cell extracts were separated by SDS-PAGE (5%–20% gradient gel, PAGEL, ATTO) and transferred to polyvinylidene difluoride membranes (Millipore). After blocking with 5% skim milk powder in PBS-T, membranes were incubated with primary antibodies, followed by incubation with horseradish peroxidase-conjugated secondary antibody. Antibodies are listed in Table S1. Densitometric semi-quantification was performed using ImageJ software.

RNA extraction and RT-qPCR
Total RNA was extracted using RNeasy Mini Kit (Qiagen) and cDNA synthesized using the SuperScript IV First-Strand Synthesis System (Thermo Fisher Science) according to the manufacturers' guidelines. Quantitative real-time PCR was carried out using the FastStart Essential DNA Green Master (Roche) and LightCycler 96 (Roche). All primer sequences are as followed; *GAPDH* (forward: 5′-CTGACTTCAACAGCGACACC-3′; reverse: 5′-TAGCCAAATTC GTTGTCATACC-3′), *CCND1* (forward: 5′-GCTGTGCATCTACA CCGACA-3′; reverse: 5′-TTGAGCTTGTTCACCAGGAG-3′) and *CCND2* (forward: 5′-GGACATCCAACCCTACATGC-3′; reverse: 5′-CGCACTTCTGTTCCTCACAG-3′). The $2^{-\Delta\Delta Ct}$ method was used to determine relative gene expression.

5-Ethynil-2′-deoxyuridine administration
5-Ethynil-2′-deoxyuridine (EdU) labeling was performed by intraperitoneally injecting EdU (Abcam) into pregnant ICR mice at E13.5, as previously described.[24] Embryos were harvested 24 h post injection and processed for sectioning and staining for EdU and other primary antibodies of interest. For EdU staining, sections were incubated at room temperature with a solution containing 150 mM NaCl, 50 mM Tris buffer (pH 7.5), 2 mM $CuSO_4$ (II), 2 μM Alexa Fluor azide (Life Technologies), and 10 mM sodium ascorbate in distilled water for 2 h and then washed with PBS.

Tissue harvest and sectioning
For the harvest of embryos, pregnant mice were deeply anesthetized with isoflurane and the embryos were removed, decapitated, and the heads were immersed in 4% paraformaldehyde overnight at 4°C and then in 10%, 20%, and 30% sucrose solutions. Postnatal mice were deeply anesthetized with isoflurane and the heart was subsequently perfused with fresh 2 mL/g PBS followed by 4% paraformaldehyde (Fujifilm, Wako Pure Chemical Crop). The organs of interest were harvested, followed by immersion in the same fixative overnight at 4°C, and then in 10%, 20%, and 30% sucrose solutions (Fujifilm, Wako Pure Chemical Crop). After replacement with sucrose solutions, organs were embedded and frozen in SCEM (Super Cryoembedding Medium, SECTION-LAB Co., Ltd.). Brain, kidneys, and female reproductive systems were sectioned at 20-μm thickness for immunohistochemistry. For Nissl and hematoxylin and eosin staining, the dissected and post-fixed organs were dehydrated in ethanol and embedded in paraffin, followed by sectioning at 4 μm thickness.

Immunohistochemistry
For immunohistochemistry, cryo-sectioned tissues were incubated in a blocking solution of 0.5% Triton X-100 in Blocking One (Nacalai Tesque, Inc.) at room temperature for 60 min and then reacted with primary antibodies of interest at 4°C for 16–24 h. Samples were then washed with PBS-T and stained with secondary antibody and DAPI at 4°C for 2 h. After final washing with PBS, the stained samples were sealed with mounting medium and visualized by either confocal microscopy (Zeiss Axio Observer) or fluorescence microscopy (Nikon A1RS+). The antibodies used are listed in Table S1.

Statistical analysis
Results are presented as the mean ± SEM. A two-sided Student t test with Welch's correction was performed to compare the means between two groups. When the means of three groups were compared, a one-way ANOVA with a Geisser-Greenhouse correction followed by post hoc Dunnett's multiple comparison test was used. Statistics were calculated using EZR (Saitama Medical Center, Jichi Medical University).[25] A p value of <0.05 was considered to indicate a significant difference.

Study approval
Written informed consents for publication of patient clinical features and analyses of DNA samples were obtained from the patients' parents. The use of the photograph of patients 1 and 2 was also permitted with written informed consent from the parents. All study protocols were approved by Nagoya City University Institutional Review Board and all experiments conform to the relevant regulatory standards.

Results

Exome sequencing identified two additional candidates with MYCN gain-of-function variants
Using GeneMatcher and international collaborations,[26] we identified two unrelated candidates with *MYCN* variants with possible gain-of-function properties who shared clinical features with a previously reported patient (summarized in Table 1).

Table 1. Comparison of clinical features in patients with MYCN gain-of-function-induced megalencephaly syndrome, MMPH, and Feingold syndrome

	MYCN gain-of-function-induced megalencephaly syndrome			MPPH3	Feingold syndrome
	Previous patient	Patient 1	Patient 2		
Variant (NM_005378.6)	c.173C>T; p.Thr58Met	c.179C>T; p.Pro60Leu	c.173C>T; p.Thr58Met	CCND2 gain-of-function	MYCN loss-of-function
Intellectual disability	severe	NA	+	mild to severe	mild learning deficiency
Motor delay	+	NA	+	+	+
Postnatal growth retardation	+	NA	−	−	+
Brain size	megalencephaly	megalencephaly	megalencephaly	megalencephaly	microcephaly
Brain magnetic resonance imaging findings					
Ventriculomegaly	+	+	+	+	−
Hydrocephalus	−	−	−	+	−
Bilateral perisylvian polymicrogyria	−	−	−	+	−
Corpus callosum dysplasia	hypoplastic	−	hypoplastic	thick or mega	−
Congenital heart disease	VSD	ND	−	±	±
Digital anomalies					
Postaxial polydactyly	+	+	+	+	−
Toe syndactyly	−	−	−	−	+
Brachymesophalangy	−	−	−	−	+
Tracheal dysplasia	tracheomalacia	−	−	−	tracheoesophageal fistula
Gastrointestinal atresia	−	−	−	−	±
Others	Neuroblastoma diagnosed at 7 mo. Remission as of 19 y	Clinical information limited because of artificial abortion	Neuroblastoma diagnosed at 3 mo. Remission as of 1 year 7 mo	NA	NA

MPPH, megalencephaly-polymicrogyria-hydrocephalus syndrome; NA, not applicable; ND, not documented; VSD, ventricular septal defect.

Patient 1 was a male fetus of unrelated and healthy French parents (Figure 1A). Trio-based exome sequencing identified a *de novo* heterozygous missense variant [NM_005378.6:c.179C>T; p.Pro60Leu (P60L)] in the *MYCN* gene as the top candidate without any other candidates, and the variant was subsequently confirmed by Sanger sequencing (Figure 1B). P60L substitution was not found in any public databases of the general population (e.g., gnomAD),[27] although it was present in the Catalog Of Somatic Mutations In Cancer as a somatic amino acid substitution in basal cell carcinoma of the skin.[28] Furthermore, the Pro60 residue is evolutionary conserved across species. Indeed, the variant was predicted to be pathogenic and damaging by *in silico* analyses (Polyphen-2 score = 0.985, SIFT score = 0, and CADD phred-score = 28.6).[29] Clinically, fetal ultrasound examination in the second trimester indicated ventriculomegaly and postaxial polydactyly. Subsequent fetal brain magnetic resonance imaging (MRI) at 30 weeks of gestation confirmed the enlarged ventricle and macrocephaly, with both biparietal and fron-tal-occipital diameters greater than the 95th percentile for his gestational age (Figures 1C and 1D). He was subjected to termination of pregnancy for his multiple congenital anomalies at 31 weeks of gestation, with a body weight at the 88th percentile and a length at the 49th percentile. He showed post-axial polydactyly of both hands (Figures 1E and 1F), facial dysmorphism with hypertelor-ism, a short nose with anteverted nares, low-set ears, and retrognathia (Figures 1G and 1H). The autopsy showed a Meckel's diverticulum and left pyeloureteral dilatation. Pathological analysis of the fetal brain identified a brain weight >95th percentile (megalencephaly) and a right enlarged ventricle, but no clear polymicrogyria.

Patient 2 was an 8-month-old Japanese boy born to non-consanguineous healthy parents (Figure 1I). We identified the same variant as in our previously reported patient, a *de novo* missense variant [NM_005378.6:c.173C>T; p.Thr58Met (T58M)] (Figure 1J). The boy exhibited mega-lencephaly, postaxial polydactyly, and dysmorphic facial gestalt, which were the same phenotypes as those found
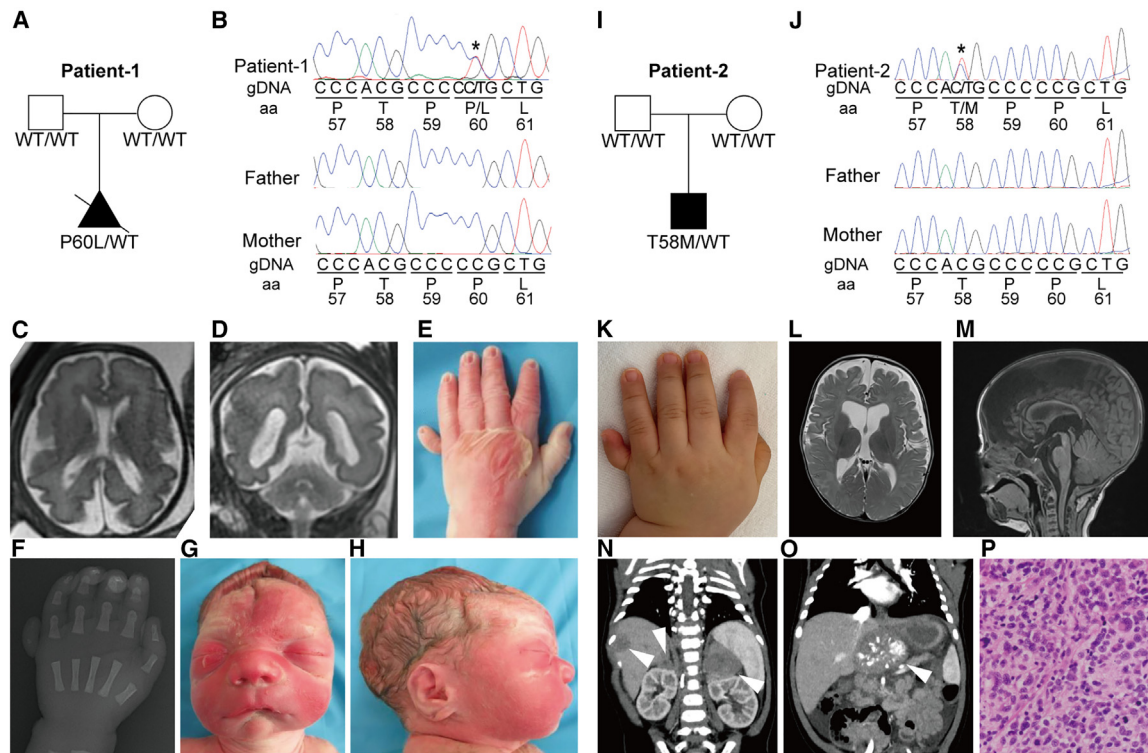
**Figure 1. Genetic analysis and clinical features of the patients**

(A) Pedigree analysis of patient 1. The genotype of the variant, p.Pro60Leu (P60L), or WT in the *MYCN* gene is given.

(B) Sanger sequence for patient 1. The asterisk indicates the base substitutions in a heterozygous state.

(C and D) Axial and coronal slices of T2-weighted MR images acquired at 30 weeks of gestation showing megalencephaly and ventriculomegaly.

(E) The representative pictures of postaxial polydactyly in patient 1.

(F) X-ray image showing postaxial polydactyly.

(G and H) Representative pictures of patient 1, who was subjected to termination of pregnancy at 31 weeks of gestation. Distinctive facial features of a posteriorly rotated ear, hypertelorism, and a wide and depressed nasal bridge were observed.

(I) Pedigree analysis of patient 2. The genotype of the variant, p.Thr58Met (T58M) or WT in the *MYCN* gene is given.

(J) Sanger sequence of patient 2. The asterisk indicates the base substitutions in a heterozygous state.

(K) Representative pictures of postaxial polydactyly in patient 2.

(L and M) Axial and sagittal slices of T2-weighted MR images showing megalencephaly, ventriculomegaly and hypoplastic corpus callosum.

(N and O) Contrast-enhanced computed tomography images showing tumors in the bilateral adrenal glands, liver and in front of a vertebrae (arrow head).

(P) Hematoxylin and eosin (H&E) staining of the tumor showing the appearance of a neuroblastoma.

in patient 1 and the previously reported patient (Figure 1K). Brain MRI showed an enlarged ventricle and hypoplastic corpus callosum (Figures 1L and 1M). Furthermore, as with the previous patient diagnosed with neuroblastoma at the age of 7 months, a tumor was detected at birth and subsequently classified as an intermediate-risk neuroblastoma, according to the Children's Oncology Group's risk assessment, when he was 3 months old (Figures 1N–1P). His neuroblastoma responded well to chemotherapy and surgical intervention, and was maintained under remission. Collectively, these two patients and our previous patient share common major phenotypes.

Functional analysis revealed the gain-of-function nature of the MYCN variants

We hypothesized that the P60L substitution was a gain-of-function variant as it is located close to T58 and may adversely affect phosphorylation at T58, as observed with the T58M substitution, leading to reduced MYCN degradation and subsequent protein accumulation. To test this hypothesis, we transfected plasmids expressing MYCN-WT, MYCN-T58M, and MYCN-P60L in HEK293T cells and semi-quantified the level of phosphorylation at T58 and the stability of the MYCN protein. First, the level of T58-phosphorylation was significantly lower in both MYCN-P60L and MYCN-T58M transfected cells compared with MYCN-WT transfected cells (Figures 2A and 2B). Next, to test whether decreased phosphorylation at T58 stabilized the mutant protein, we co-transfected plasmids in HEK293T expressing either MYCN-WT, MYCN-T58M, or MYCN-P60L together with those expressing F box and WD repeat domain-containing 7 (Fbw7; Myc-tag), the ubiquitin ligase targeting MYCN.[30] Both MYCN-P60L and MYCN-T58M were shown to be more stable than MYCN-WT
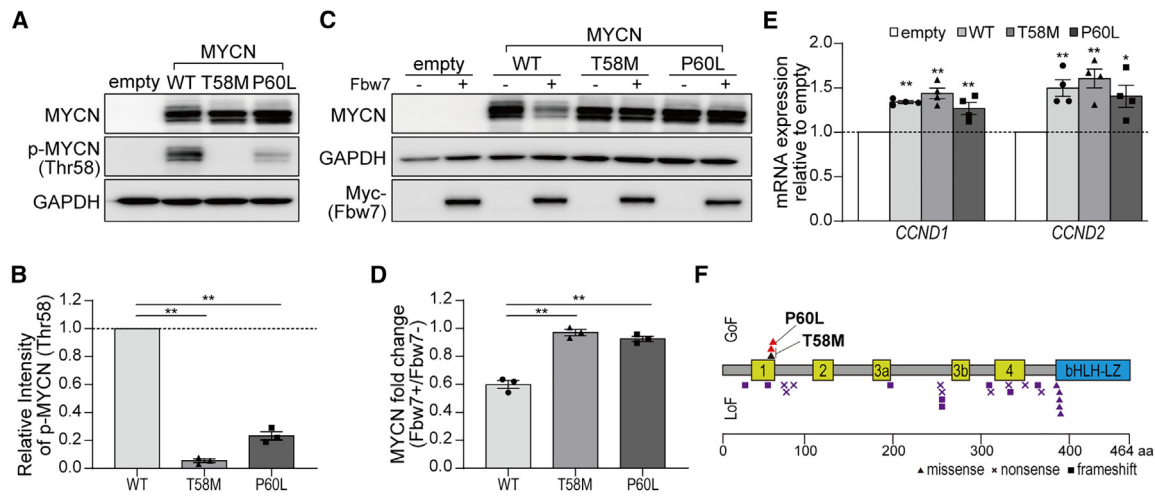
Figure 2. Effect of the p.P60L variant on MYCN stability and its downstream targets

(A and B) Expression of MYCN-WT, MYCN-T58M, and MYCN-P60L cells in HEK293T cells. Lysates of cells transfected with MYCN-WT, MYCN-T58M, or MYCN-P60L plasmids were subjected to sodium dodecyl sulfate-polyacrylamide gel electrophoresis, followed by western blotting with anti-N-Myc, phospho-c-Myc (pThr58) or glyceraldehyde-3-phosphate dehydrogenase (GAPDH) antibodies. The intensity of p-MYCN (Thr58) was significantly lower for both T58M and P60L. Relative intensity of p-MYCN expression with respect to MYCN expression was normalized to MYCN-WT from three independent experiments.

(C and D) Expression of MYCN in HEK293T transfected with the same plasmids above with or without F box and WD repeat domain-containing 7 (Fbw7), showing that MYCN-P60L acquired stability to an equivalent extent, even in the presence of Fbw7. Fold change of MYCN (Fbw7+) relative to MYCN (Fbw7−) was significantly increased for MYCN-T58M and MYCN-P60L compared to MYCN-WT from three independent experiments.

(E) Transcriptional levels of Cyclin D1 (CCND1) and CCND2 with qRT-PCR for RNA extracted from HEK293T cells transfected with the same plasmids above. For MYCN-WT, MYCN-T58M or MYCN-P60L, the transcriptional levels of CCND1 and 2, that are MYCN downstream targets, were equivalent to those of MYCN-WT. Transcriptional levels of CCND1 and CCND2 relative to those of GAPDH were normalized to empty vector from three independent experiments. For bar graphs and scatterplots, means and SEM are shown; *p < 0.05, **p < 0.01. Dotted lines indicate a ratio of 1.0.

(F) Schemic diagram of MYCN protein structure and the variants' loci based on NM_005378.6 reference sequence. The functional domains, MYC boxes (yellow boxes) 1–4 and the basic helix-loop-helix-leucine-zipper (bHLH-LZ, blue box), are shown. The variants are colored as red (present patients, p.Thr58Met [T58M] and p.Pro60Leu [P60L]), black (previous patient) and purple (patients with Feingold syndrome 1 reported in ClinVar) and represented as triangle (missense substitutions), "x" (nonsense variants), and square (small indels leading to FS). Gain of function (GoF) variants and loss of function (LoF) variants are indicated above and below the protein structure, respectively.

(Figures 2C and 2D). Last, we evaluated the transcriptional activities of the mutant MYCN proteins to test whether the mutant MYCN proteins had diminished canonical activity as a transcription factor. Both MYCN-P60L and MYCN-T58M maintained their abilities to activate transcription of the downstream genes, CCND1 (MIM: 168461) and CCND2, in a similar manner to MYCN-WT (Figure 2E). Thus, we demonstrated that MYCN-P60L exerted gain-of-function abilities caused by increased stability and avoiding degradation mediated by Fbw7-mediated ubiquitination, as was observed in the MYCN-T58M mutant. Analysis of the clinical and functional data confirms MYCN gain-of-function variants as the cause of this megalencephaly-polydactyly syndrome, with symptoms that are mirror phenotypes of those caused by MYCN loss-of-function variants in Feingold syndrome (Figure 2F).

Generation of Mycn gain-of-function and loss-of-function mice and characterization

To further elucidate the function of Mycn during development, we generated Mycn gain-of-function and loss-of-function mouse models. For the gain-of-function mouse model, we produced mice heterozygous for T58M analogous to the patients with the megalencephaly-polydactyly syndrome. For the loss-of-function mice, we introduced two base deletions at highly conserved sequences of exon 1 to induce a frameshift (FS). We confirmed the intended genomic alterations by Sanger sequencing (Figure S1A). For analyses, we focused on heterozygous gain-of-function mice (T58M/WT) and haploinsufficient mice (FS/WT) because of the heterozygous genotypes of the patients. Furthermore, we mainly analyzed female mice, which never experienced pregnancy, because male mice were mostly euthanized for their sperm for use in in vitro fertilization.

Heterozygous T58M/WT and FS/WT mice were born at a Mendelian ratio. We validated the decreased phosphorylation at T58 and subsequent accumulation of Mycn protein in T58M/WT mice (Figures 3A and 3B), and the lower expression of Mycn in FS/WT mice (Figures 3C and 3D). Although there was no significant difference in body weight between female T58M and WT/WT mice, the body weight of female FS/WT mice was significantly lower than with littermate WT/WT controls at postnatal day 56 (P56; Figures 3E–3G). Male mice showed no difference in body weight at P28 and P56, except for a slightly lower body weight in male T58M mice at P28 (Figures S1B–S1D).
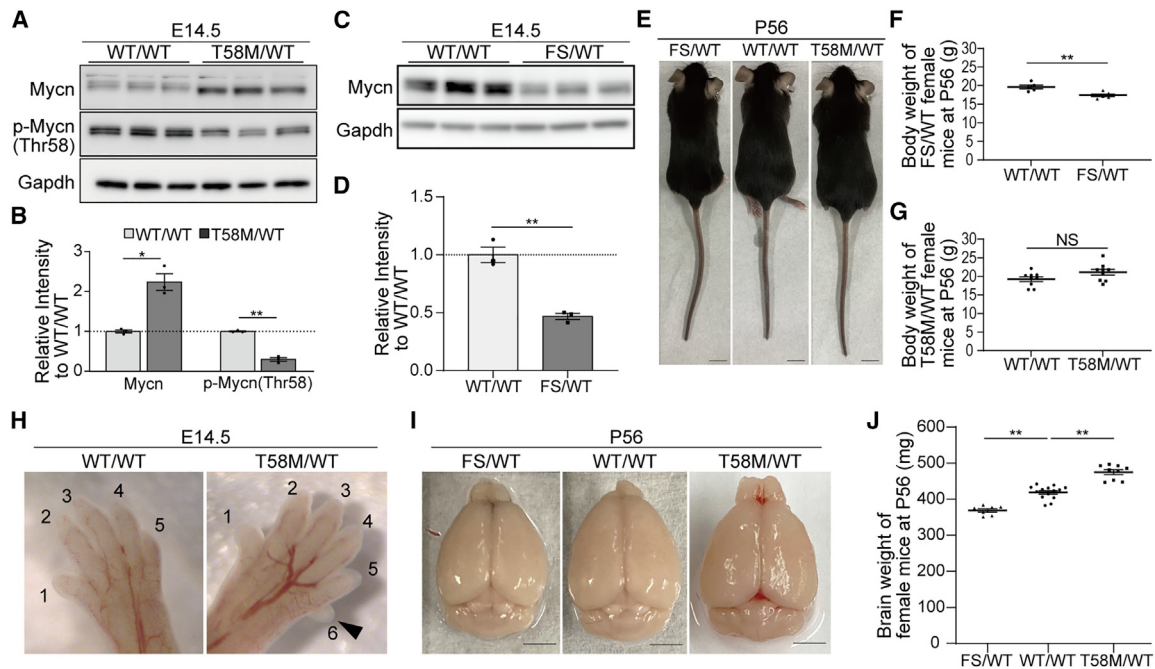
Figure 3. Generation of *Mycn* gain-of-function (T58M/WT) and haploinsufficient mice (FS/WT)
(A and B) Expression of Mycn in the cortex at E14.5. The intensity of p-Mycn (Thr58) was significantly decreased in the cortex of T58M/WT mice, resulting in a significantly increased expression of Mycn. Relative intensities of Mycn to Gapdh and p-Mycn (Thr58) to Mycn expression were normalized to Mycn-WT among three biological replicates.
(C and D) Expression of Mycn in the cortex at E14.5. The intensity of Mycn was significantly lower in the cortex of FS/WT mice. Relative intensities of Mycn to Gapdh were normalized to Mycn-WT among three biological replicates.
(E) Representative images of the whole body at P56.
(F and G) Body weight at P56. The body weight of female FS/WT mice was significantly decreased compared with littermate WT/WT controls, while that of female T58M/WT and WT/WT mice were not different to each other (WT/WT, n = 5; FS/WT, n = 6; and WT/WT, n = 9; T58M/WT, n = 9).
(H) Representative images of the forelimb of WT/WT and T58M/WT mice at E14.5. T58M/WT mice exhibited postaxial polydactyly.
(I and J) Representative images of the brain and its weight at P56. The brain weight of T58M/WT mice was significantly larger, and that of FS/WT mice significantly lower, compared with WT/WT mice (female data shown; WT/WT, n = 14; FS/WT, n = 7; T58M/WT, n = 9). For bar graphs and scatterplots, means and SEM are shown; *p < 0.05, **p < 0.01. NS, not significant. Dotted lines indicate a ratio of 1.0.

Although FS/WT mice did not show overt abnormalities of the digits, more than 90% of T58M/WT mice exhibited postaxial polydactyly at embryonic day 14.5 (E14.5; Figures 3H and S1E). Both T58M/WT and FS/WT mice showed no morphological brain abnormalities (Figure 3I), but brain weights were significantly lower in FS/WT, and higher in T58M/WT mice, compared with WT/WT mice at P56 (Figure 3J). In addition, both male and female mice carrying the T58M/WT genotype were incapable of achieving natural breeding, although FS/WT mice were fertile and bred normally. There were no overt abnormalities regarding viability or apparent behavioral development.

Mycn-T58M/WT mice exhibited thickened cerebral cortex with an increased number of neurons
To elucidate the histological changes in the central nervous systems, we evaluated Nissl staining of the cerebrum and cerebellum at P56. Although there were no overt morphological changes, the thickness of the cerebral cortex in the primary motor cortex, especially cortex layers II–III, was significantly affected, being thinner in FS/WT mice and thicker in T58M/WT mice (Figures 4A–4D).

Moreover, the cerebellum was also enlarged, with the area of cerebellar vermis significantly larger in T58M/WT and smaller in FS/WT, compared with WT/WT mice (Figures 4E and 4F). To clarify the cause of megalencephaly, we evaluated the number of neuronal cells, revealing that the number of Neun+ cells was significantly higher in T58M/WT mice and lower in FS/WT mice, suggesting over- and under-proliferation of neuronal progenitors, respectively, during neurogenesis at an early developmental stage (Figures 4G–4I).

We then evaluated the T58M/WT mice at P0 and P7 to determine whether the phenotype in the central nervous system had already been determined toward megalencephaly around birth. Although T58M/WT mice exhibited no significant differences in body weight at P0 and P7 (Figure 5A), the brain weight was significantly heavier in T58M/WT mice at P0 and P7, compared with WT/WT mice (Figure 5B). Moreover, we evaluated the thickness of each cortex layer, showing that the thickness of the total cortex layer and layers VI were significantly thicker in T58M/WT mice (Figures 5C–5E). Furthermore, the number of neurons in cortex layers II–IV, labeled with Satb2, and
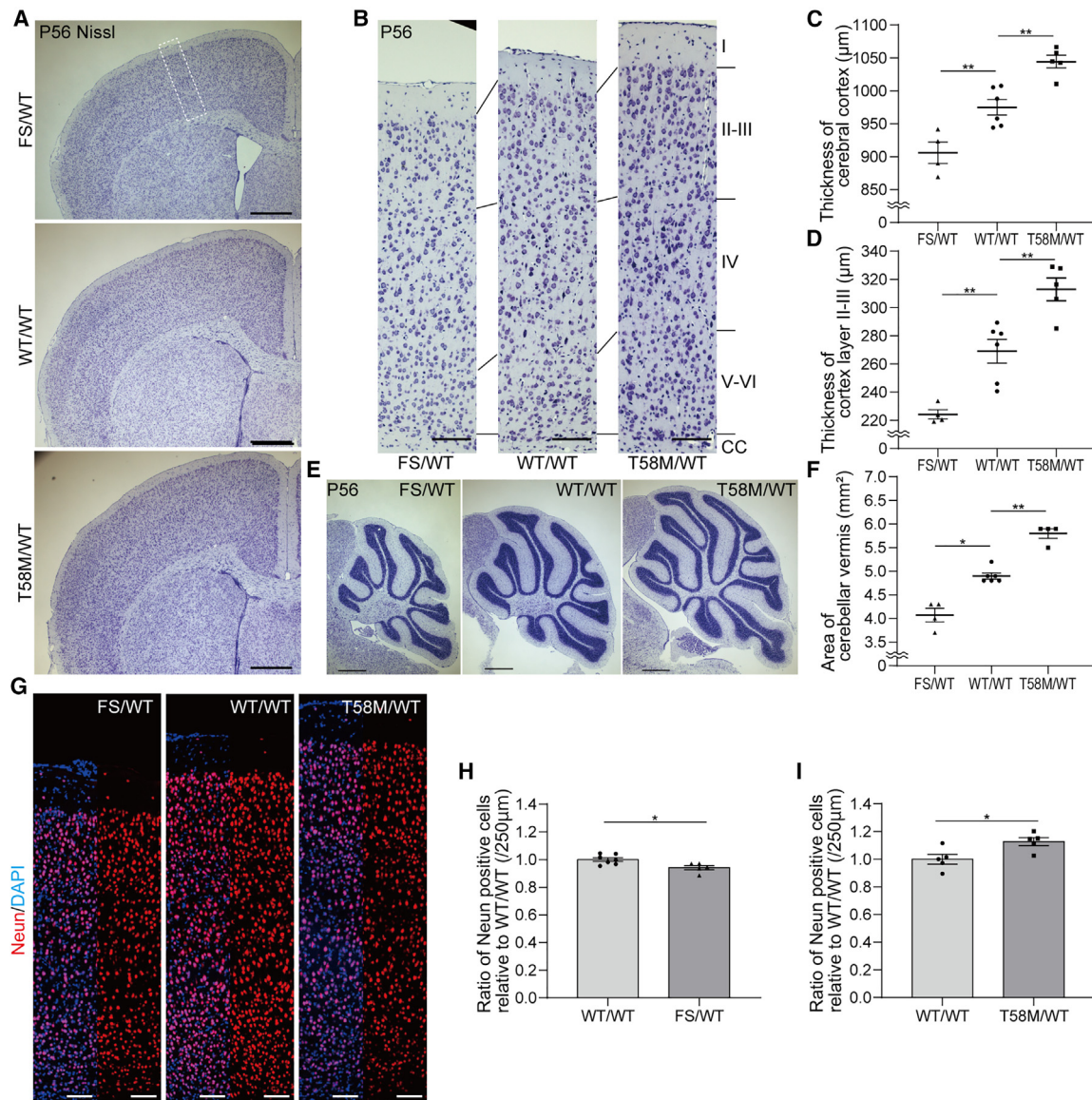
Figure 4. Effect of *Mycn* gain of function and haplo-insufficiency on postnatal neurological phenotypes

(A and B) Representative images of Nissl staining of the cortex of mice harvested at P56. The primary motor cortex, indicated by a white dotted square, is magnified and each of the cortex layers is indicated with black lines. The photographs were taken at low, 2.5× (A), and high, 10× (B), magnification under bright-field illumination with a ZEISS Axio Observer Z.1 inverted microscope (Carl Zeiss). Scale bars, 500 μm (A) and 100 μm (B). CC, corpus callosum.

(C and D) Quantification of the cortex thickness showing a significantly thicker cerebral cortex and cortex layers II–III in T58M/WT mice, and significantly thinner cerebral cortex and cortex layers II–III in FS/WT mice, compared with WT/WT mice (female data shown; WT/WT, n = 6; FS/WT, n = 4; T58M/WT, n = 5).

(E) Representative pictures of Nissl staining of the cerebellar vermis of mice harvested at P56. The photographs were taken at 2.5× magnification under bright-field illumination. Scale bar, 500 μm.

(F) Quantification of the area of cerebellar vermis. The area of the vermis was significantly larger for T58M/WT mice, and significantly smaller for FS/WT, compared with WT/WT mice (female data shown; WT/WT, n = 6; FS/WT, n = 4; T58M/WT, n = 4).

(G) Representative cerebral cortex images of mice harvested at P56, immunostained for Neun (red) and DAPI (blue). The photographs were taken at 10× magnification with a Nikon A1RS + confocal microscope. Scale bar, 100 μm.

(H and I) Quantification of the ratio of Neun+ cells in the cerebral cortex compared with littermate WT/WT mice, showing that the ratio of Neun+ cells was significantly lower in FS/WT mice and higher in T58M/WT mice (WT/WT, n = 7; FS/WT, n = 5; and WT/WT, n = 5; T58M/WT, n = 5). For bar graphs and scatterplots, means and SEM are shown; *p < 0.05, **p < 0.01.

the number at layer VI, labeled with Tbr1, were significantly larger in T58M/WT mice (Figures 5F and 5G), indicating that the fate had been determined toward megalencephaly before birth.

Neurogenesis in Mycn-T58M/WT mice is increased

We previously reported that Mycn over-expression results in delayed cell-cycle exit and neuronal migration delay.[16] To determine whether those pathological events
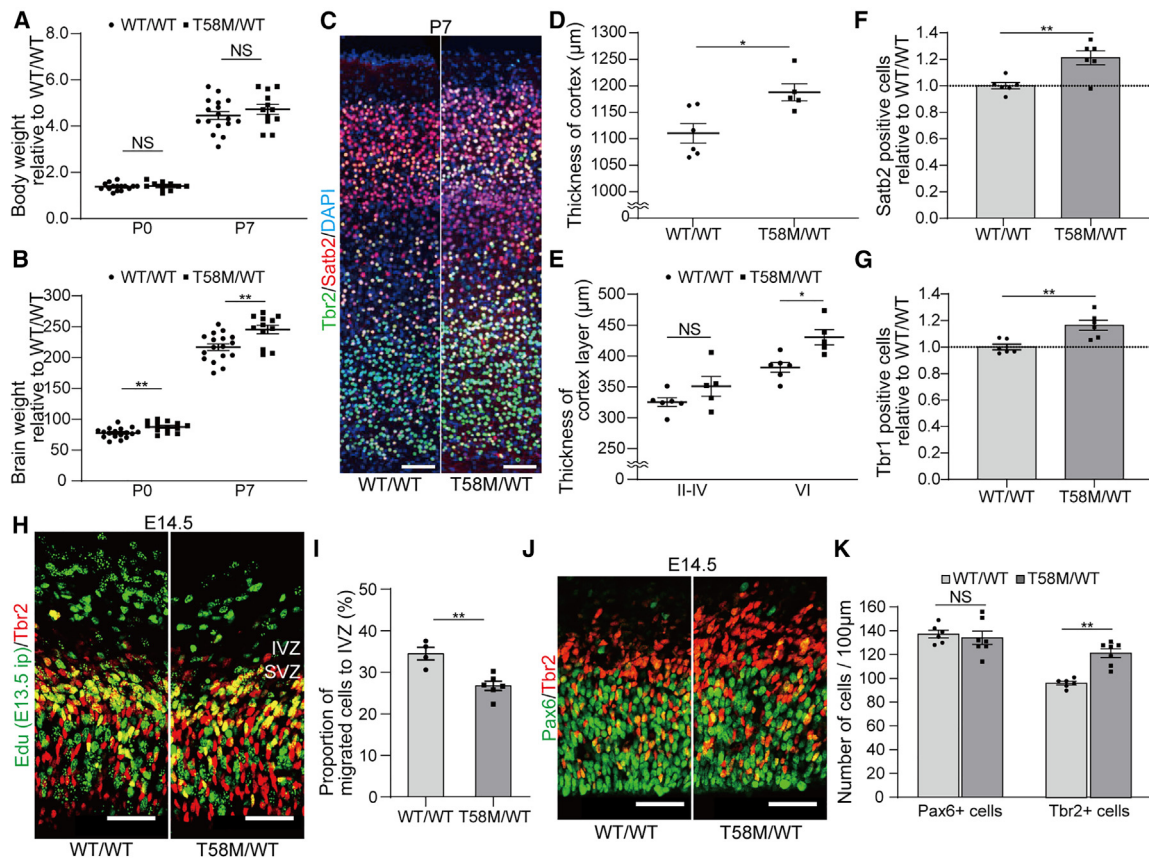
Figure 5. Perinatal neurological phenotypes of *Mycn* gain-of-function

(A) Body weights at P0 (WT/WT, n = 10; T58M/WT, n = 15) and P7 (WT/WT, n = 12; T58M/WT, n = 17) were not different between WT/WT and T58M/WT mice.

(B) At both P0 and P7, the brain weights of T58M/WT (P0, n = 13; P7, n = 12) were significantly heavier than those of WT/WT (P0, n = 17; P7, n = 17).

(C) Representative cerebral cortex images of mice harvested at P7, immunostained for Tbr2 (green), Satb2 (red) and DAPI (blue). The photographs were taken at 10× magnification with a Nikon A1RS + confocal microscope. Scale bar, 100 μm.

(D and E) Quantification of the thickness of the cerebral cortex and cortex layers II–IV and VI. The total thickness of the cerebral cortex and the thickness of layer VI were significantly thicker in T58M/WT mice (WT/WT, n = 6; T58M/WT, n = 5).

(F and G) Quantification of the relative number of Satb2+ and Tbr1+ neurons in T58M/WT to that in WT/WT. The ratios were significantly higher in T58/WT mice (WT/WT, n = 6; T58M/WT, n = 6).

(H) Representative coronal sections of developing cortex harvested at E14.5, immunostained for EdU (green) and Tbr2 (red). EdU was intraperitoneally injected in mothers bearing E13.5 embryos. The photographs were taken at 40× magnification with a Nikon A1RS + confocal microscope. Scale bar, 50 μm.

(I) Quantification of the number of EdU+ cells in the intermediate zone (IVZ) relative to total EdU+ cells showing a significantly reduced proportion of EdU+ cells in the IVZ, indicating delayed migration of IPCs (WT/WT, n = 4; T58M/WT, n = 6).

(J) Representative coronal sections of the developing cortex harvested at E14.5, immunostained for Pax6 (green) and Tbr2 (red). The photographs were taken at 40× magnification with a Nikon A1RS + confocal microscope. Scale bar, 50 μm.

(K) Quantification of the number of Pax6+ and Tbr2+ cells in the ventricular zone and subventricular zone (SVZ). Although the number of Pax6+ cells was unchanged, the number of Tbr2+ cells in T58M/WT was significantly larger compared with WT/WT (WT/WT, n = 6; T58M/WT, n = 7). For bar graphs and scatterplots, means and SEM are shown; *p < 0.05, **p < 0.01. NS, not significant. Dotted lines indicate a ratio of 1.0.

occurred *in vivo* and to assess the underlining mechanism of megalencephaly observed as early as P0 and P7 in T58M/WT mice, we analyzed neuronal migration and the number of intermediate neural precursors (IPCs) at E13.5 and E14.5. First, we analyzed neuronal migration by labeling the mitotic IPCs at E13.5 and detecting those cells at E14.5. As a result, the number of EdU-labeled cells migrating to the intermediate zone was significantly lower in T58M/WT mice (Figures 5H and 5I), consistent with the delayed exit of the cell-cycle

and migration delay seen *in vitro*. Next, we harvested embryos at E14.5, and in agreement with the cell-cycle assessment during neurogenesis, the number of IPCs increased significantly, while the number of Pax6+ radial glia did not change (Figures 5J and 5K). Overall, a gain of *Mycn* function and subsequent protein accumulation may cause excessive proliferation of IPCs and an ensuing delayed neuronal migration, leading to postnatal megalencephaly with an increased number of neurons.
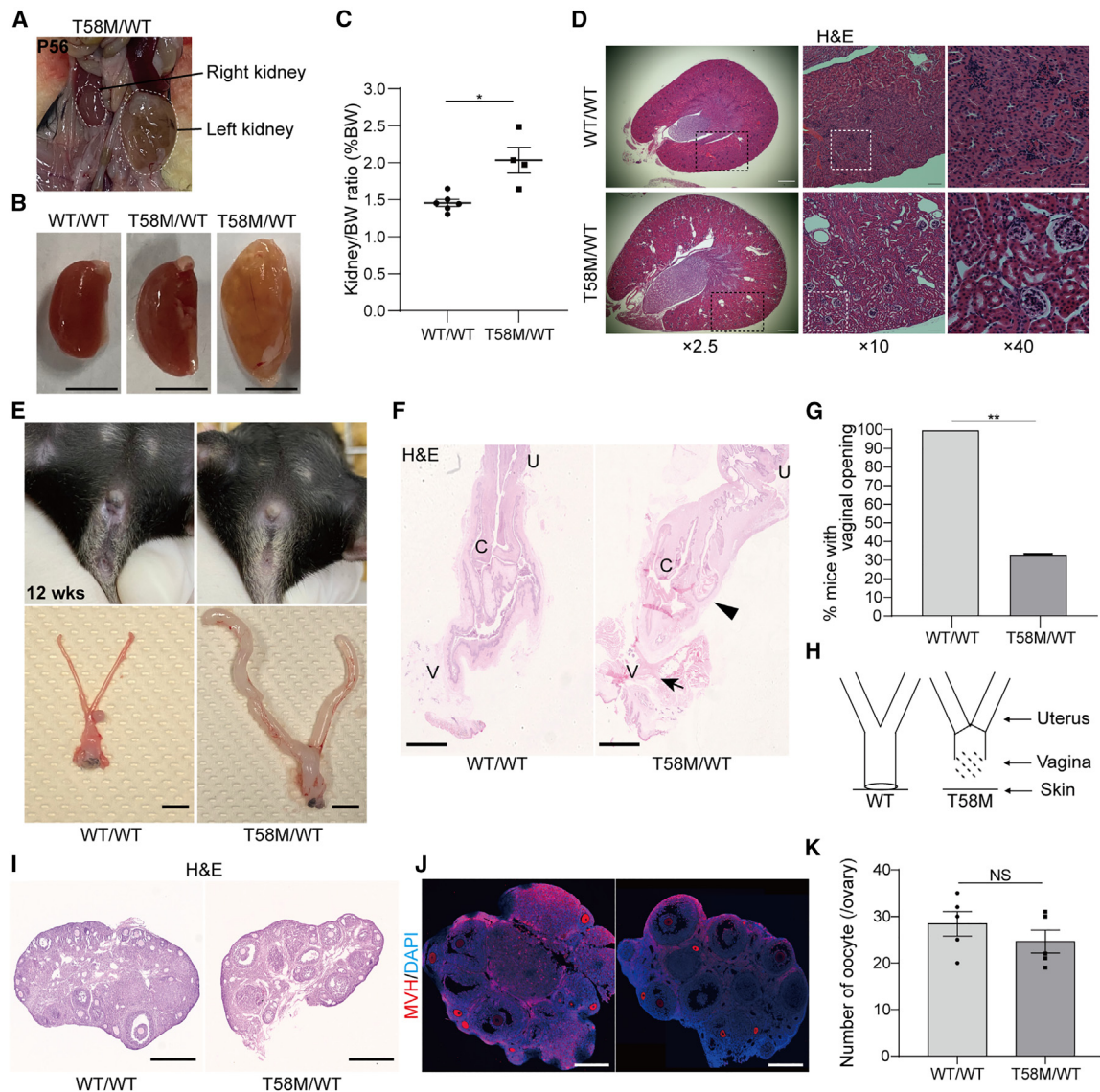
Figure 6. *Mycn* gain-of-function mutation adversely affects the development of organs other than the brain

(A and B) (A) Macroscopic images of intraabdominal organs at P56, with kidneys indicated by white dotted lines, and (B) dissected kidneys of WT/WT and T58M/WT. The kidneys were enlarged and macroscopically cystic in the right panel.

(C) Kidney weight relative to body weight was higher in T58/WT (n = 4) compared with WT/WT (n = 6).

(D) Representative images of hematoxylin and eosin (H&E) staining of WT/WT and T58M/WT kidneys. Even those kidneys that were not macroscopically cystic displayed microscopically cystic renal tubules. Scale bar represents 500 μm (left), 100 μm (center panel) and 25 μm (right).

(E) Macroscopic images of the vagina and dissected uterine tract. Upon visual inspection, the vagina seemed to be closed, and, after dissection, the presence of hydrometra in both the vagina and uterus of T58M/WT mice was observed. Scale bar, 1 cm.

(F) H&E staining of the uterovaginal canal, showing a blind uterus (arrow head) and vaginal atresia with hyperkeratotic epithelium forming a block at the distal end (arrow) in T58M/WT mice. C, cervix; U, uterus; V, vagina.

(G) The proportion of mice with a vaginal opening (WT/WT, n = 8; T58M/WT, n = 9).

(H) Schematic image of the uterovaginal phenotype, showing that T58M/WT mice have an imperforate vagina with or without a blind uterus.

(I) H&E staining of the ovary shows no morphological changes.

(J and K) Mouse Vasa homologue staining (red) of WT/WT (n = 5) and T58M/WT ovaries (n = 5) indicates no difference in oocyte counts between the genotypes. For bar graphs and scatterplots, means and SEM are shown; *p < 0.05, **p < 0.01. NS, not significant.

Mycn gain-of-function mutation perturbs the development of organs other than brain

We next focused on the development of organs other than the brain. Macroscopically, there were no detectable morphological abnormalities in the heart, lung, liver, intestine and colon. In addition, there was no difference in the weight of the median lobe of the liver between T58M/WT and WT/WT mice (Figure S1F). In contrast, the kidney and uterus showed overt morphological changes. Given these observations and the *Mycn* expression pattern,

we focused on the phenotypes in the kidney and female reproductive tract. First, we analyzed the kidney because of the *MYCN* expression pattern in human kidneys. The kidneys were enlarged in T58M/WT mice and the relative kidney weight to body weight was significantly larger than in WT/WT mice (Figures 6A–6C). Interestingly, one out of six mice analyzed showed an apparent unilateral cystic kidney (Figure 6A), and two mice had a single unilateral kidney. Histological analysis revealed dilatation of the renal convoluted tubules, indicating an over-proliferation of renal tubule cells (Figure 6D). Next, we focused on the female reproductive tract, because all female T58M/WT mice were infertile. Macroscopically, hydrometra was observed in T58M/WT mice and 30% of T58M/WT mice had an open vagina (Figures 6E–6G), indicating an imperforate vagina. Histologically, the uterovaginal canal showed a blind uterus and vaginal atresia with hyperkeratotic epithelium forming a blockage at the distal end inT58M/WT mice (Figures 6F and 6H). No obvious morphological differences in ovarian size or structure were observed in T58M/WT mice, and mouse Vasa homologue staining revealed no difference in oocyte counts between the genotypes (Figures 6I–6K). In summary, MYCN plays an essential role in organogenesis, not only of the central nervous system, but also of the kidney and female reproductive system, and the diverse non-brain phenotypes are suggested to be attributed to the over-proliferation of tissues forming these organs.

Discussion

In the present study, through the identification of two additional patients and cellular and pathophysiological analyses using mouse models, we have detailed a *MYCN* gain-of-function-induced megalencephaly-polydactyly syndrome, which shows mirror phenotypes to Feingold syndrome caused by loss-of-function *MYCN* variants. With the analysis of *Mycn* gain- and loss-of-function mouse models, we revealed the maldevelopment of multiple organs, including the central nervous system, kidney and female reproductive system. This was caused by over-proliferation of the tissues comprising those organs and underscores the importance of MYCN during organogenesis. In addition, although no tumor was detected in the mouse models, the over-proliferation observed in multiple tissues could predispose to tumorigenesis and tumor progression, with or without the additional burden of other mutations. Collectively, our findings clearly show that over-active MYCN exerts detrimental effects, both on the development of multiple organs and on possible tumorigenesis and its progression.

The phenotypic characterization of our two patients, along with our previous patient with an MYCN gain-of-function variant, showed specific clinical features shared by the patients and thus this megalencephaly-polydactyly syndrome could be a recognizable syndrome. All patients showed megalencephaly and ventriculomegaly, but without the polymicrogyria seen in patients with MPPH3, along with postaxial polydactyly and dysmorphic facial features, such as hypertelorism, a wide and depressed nasal bridge, a wide nasal base, and an upturned nasal tip. Interestingly, all three cases with *MYCN* gain-of-function variants showed a hypoplastic corpus callosum despite a megalencephalic cerebrum, which is considered one of the characteristic radiological features distinguishing it from other megalencephalic syndromes. Moreover, it is noteworthy that two of the patients developed neuroblastoma during their infancy, and this syndrome should not be considered just as a genetic syndrome with multiple congenital anomalies without any definitive treatment, but as one of the hereditary neoplastic syndromes that should be recognized as early as possible for early detection and intervention for any tumors. For early recognition of the syndrome, the comprehensive phenotypic characterizations reported here are of great value; however, further characterization with emerging patients is still warranted.

Gain-of-function *Mycn* mice have not been generated and pathophysiologically analyzed before. However, analysis of a sonic hedgehog (Shh) over-expression model, whose pathway includes Mycn,[31] was performed where over-expression of Shh induced prolonged proliferation of granule cell precursors (GCPs) in the cerebellum, leading to enlargement of the overall size of the cerebellum.[32] The mechanism for eliciting an over-proliferation of GCPs is likely to include Shh induction of its direct target, Mycn, resulting in cell-autonomous G1 cyclin up-regulation and subsequent GCP proliferation.[32] Because the targets of Shh that participate in the proliferation of cerebellar GCPs are not limited to Mycn, this more specific analysis using the *Mycn* gain-of-function model is of great importance for a better understanding of the molecular pathomechanisms of cerebellar development.

Through the generation of *Mycn* gain-of-function mice, we have demonstrated increased IPCs with a neuronal migration delay in T58M/WT mice that is consistent with previous results, showing an over-expression of Mycn results in a delayed cell-cycle exit accompanied by delayed neuronal migration.[16] In addition to the indirect evidence that Shh over-expression induces over-proliferation of neuronal cells, MYCN itself has been reported to control and regulate the balance between symmetrical and asymmetrical cell division (SCD and ACD) in neuroblastoma cells,[33] and over-expression of MYCN induces SCD despite decreased expression causing ACD, which seems to be associated with neuroblastoma tumorigenesis.[33] The balance between SCD and ACD is not only important for tumorigenesis and progression, but is also fundamental for tissue homeostasis and the proper development of various organs.[34] For example, in neurogenesis, the balance is important for maintaining the proper number of generated neurons.[35] The more cell cycles in which the neural progenitors divide symmetrically, the later they exit the cell cycle, and the greater the increase in the total

number of neurons, resulting in clinical brain megalencephaly.[36,37] This suggests that over-active Mycn induces the neural progenitors in our megalencephalic mouse model to undergo an excessive number of cell cycles with SCD, subsequently producing the increased number of mature neurons in the megalencephalic brain.

In addition to the central nervous system manifestations, we have shown morphological manifestations in multiple organs of the *Mycn* gain-of-function mice, such as the digits, female reproductive system, and kidney. Considering that the expression pattern of MYCN covers a wide range of organs other than the brain, including limbs, heart, kidney, and lung tissues,[7,8] it is not unexpected for these organs to be affected in our mouse model. In the digits, more than 90% of mice exhibited postaxial polydactyly. A previous report revealed that Shh signaling contributes to limb development by two distinct mechanisms: formation of the anterior-posterior axis for specifying each digit and proliferation of limb mesenchymal cells,[38-40] and its inactivation results in oligodactyly.[41] Accordingly, as one of the downstream targets of Shh, the digit phenotype of T58M/WT mice is possibly caused by a disturbance of the Shh signaling pathway; this concept is supported by the digit phenotypes of mouse models for Feingold syndrome, such as skeletal mesenchymal stem cell-specific *Mycn* conditional knock-out mice.[15] In the female reproductive system, we observed imperforate vagina and hydrometra caused by the closure of the vagina with over-proliferative epithelium. Shh signaling plays an important role in activating Müllerian epithelial cell proliferation in the uterus and vagina,[42] likely producing the histological changes in the female reproductive tract seen in our mouse model. The Shh signal also contributes to the disease progression of polycystic kidney disease,[43] and its inhibition prevents the excessive proliferation and microcyst formation in the disease.[44] Our present mouse model recapitulates previously reported Shh over-expression phenotypes of the vaginal epithelium and renal tubules, so that, among the targets of Shh signaling, Mycn is likely to play a predominant role in these over-proliferative phenotypes. From a clinical point of view, these findings, seen in organs other than the brain, have not been detected in our patients so far; therefore, it is recommended that these patients should be carefully monitored for involvement of these additional organs.

This present study has some limitations. First, although we detected developmental abnormalities in the central nervous system, kidney, and female reproductive system, the Mycn expression pattern might suggest the involvement of other organs.[7,8] Second, although expression is considered more abundant in the fetal stage than in the adult stage, it is also expressed in the subventricular zone, subgranular zone, olfactory bulb, subcallosal zone, and corpus callosum of young adult mice.[45] So, it is possible that the central nervous system phenotypes are caused not only by fetal neurogenesis, but also by adult neurogenesis; this could be clarified with inducible experimental models. Last, while we have considered cyclin D as one of the MYCN's downstream targets, contributing to the morphological manifestations in multiple organs, there could be other potential targets, up-regulated or down-regulated by MYCN, which could contribute to the pathomechanisms. For instance, NLRR1, a potentially up-regulated target, contributes to growth promotion of neuroblastoma, whereas DKK1, a potentially down-regulated target, could inhibit the Wnt/β-catenin pathway, thus regulating neuronal differentiation.[46,47] Moreover, it is worth noting that the expression level of MYC might be influenced by that of MYCN.[48] While we emphasize that changes in the expression of MYCN's direct targets constitute a major contribution to the pathogenesis, it is possible that transcriptional alterations in MYC's target genes might also play a partial role in the pathomechanisms. A comprehensive understanding of both up-regulated and down-regulated molecules through transcriptome analysis, originating from more specific cell types at various embryonic stages, remains an issue to be addressed in the future.

In conclusion, our data have established that *MYCN* gain-of-function variants induce a megalencephaly-polydactyly syndrome. We demonstrated that *MYCN*, an established proto-oncogene, plays a fundamental role in the organogenesis of multiple organs. Furthermore, our finding of excess proliferation in multiple tissues could share molecular pathways in common with tumorigenesis and progression in various tumors, so our mouse model may accelerate the understanding of MYCN's functions, not only in terms of development, but also of tumorigenesis and tumor progression.

Data and code availability

All data relevant to the study are included in the report. All *MYCN* variants reported herein have been deposited to ClinVar; SCV003843238.1; SCV003932129.1. Please contact the corresponding author, S.S., for further information.

Supplemental information

Supplemental information can be found online at https://doi.org/10.1016/j.xhgg.2023.100238.

Author contributions

K.Kato. and S.S.: concept and design of the study; Y.N., K.Kato, and S.S.: draft – main manuscript; Y.N., K.Kato, H.H.S., H.O., and S.S.: analyzed and interpreted the data; Y.N., K.Kato, H.F., S.M., A.V., T.F., S.O., C.Q., C.T., T.T., K. Kosaki, and S.S.: contributed to the clinical data; Y.N., K.Kato, H.F., S.M., A.V., T.F., S.O., C.Q., H.H.S., H.O., C.T., T.T., K. Kosaki, Y.T., and S.S.: revised the manuscript and made comments on the structure, details, and grammar of the article.

Declaration of interests

The authors declare no competing interests.

Web resources

GeneMatcher, https://www.genematcher.org.
ClinVar, https://www.ncbi.nlm.nih.gov/clinvar/.
gnomAD, https://gnomad.broadinstitute.org.
ToMMo, https://www.megabank.tohoku.ac.jp/english/.
Varsome, https://varsome.com/.

References

1. DePinho, R., Mitsock, L., Hatton, K., Ferrier, P., Zimmerman, K., Legouy, E., Tesfaye, A., Collum, R., Yancopoulos, G., Nisen, P., et al. (1987). Myc family of cellular oncogenes. J. Cell. Biochem. *33*, 257–266. https://doi.org/10.1002/jcb.240330404.

2. Bretones, G., Delgado, M.D., and León, J. (2015). Myc and cell cycle control. Biochim. Biophys. Acta *1849*, 506–516. https://doi.org/10.1016/j.bbagrm.2014.03.013.

3. Dang, C.V. (2012). MYC on the path to cancer. Cell *149*, 22–35. https://doi.org/10.1016/j.cell.2012.03.003.

4. Baluapuri, A., Wolf, E., and Eilers, M. (2020). Target gene-independent functions of MYC oncoproteins. Nat. Rev. Mol. Cell Biol. *21*, 255–267. https://doi.org/10.1038/s41580-020-0215-2.

5. Brodeur, G.M. (2003). Neuroblastoma: biological insights into a clinical enigma. Nat. Rev. Cancer *3*, 203–216. https://doi.org/10.1038/nrc1014.

6. Rickman, D.S., Schulte, J.H., and Eilers, M. (2018). The Expanding World of N-MYC-Driven Tumors. Cancer Discov. *8*, 150–163. https://doi.org/10.1158/2159-8290.Cd-17-0273.

7. Ota, S., Zhou, Z.Q., Keene, D.R., Knoepfler, P., and Hurlin, P.J. (2007). Activities of N-Myc in the developing limb link control of skeletal size with digit separation. Development *134*, 1583–1592. https://doi.org/10.1242/dev.000703.

8. Moens, C.B., Stanton, B.R., Parada, L.F., and Rossant, J. (1993). Defects in heart and lung development in compound heterozygotes for two different targeted mutations at the N-myc locus. Development *119*, 485–499. https://doi.org/10.1242/dev.119.2.485.

9. Grady, E.F., Schwab, M., and Rosenau, W. (1987). Expression of N-myc and c-src during the development of fetal human brain. Cancer Res. *47*, 2931–2936.

10. Hirvonen, H., Mäkelä, T.P., Sandberg, M., Kalimo, H., Vuorio, E., and Alitalo, K. (1990). Expression of the myc proto-oncogenes in developing human fetal brain. Oncogene *5*, 1787–1797.

11. Marcelis, C.L.M., Hol, F.A., Graham, G.E., Rieu, P.N.M.A., Kellermayer, R., Meijer, R.P.P., Lugtenberg, D., Scheffer, H., van Bokhoven, H., Brunner, H.G., and de Brouwer, A.P.M. (2008). Genotype-phenotype correlations in MYCN-related Feingold syndrome. Hum. Mutat. *29*, 1125–1132. https://doi.org/10.1002/humu.20750.

12. van Bokhoven, H., Celli, J., van Reeuwijk, J., Rinne, T., Glaudemans, B., van Beusekom, E., Rieu, P., Newbury-Ecob, R.A., Chiang, C., and Brunner, H.G. (2005). MYCN haploinsufficiency is associated with reduced brain size and intestinal atresias in Feingold syndrome. Nat. Genet. *37*, 465–467. https://doi.org/10.1038/ng1546.

13. Stanton, B.R., Perkins, A.S., Tessarollo, L., Sassoon, D.A., and Parada, L.F. (1992). Loss of N-myc function results in embryonic lethality and failure of the epithelial component of the embryo to develop. Genes Dev. *6*, 2235–2247. https://doi.org/10.1101/gad.6.12a.2235.

14. Zindy, F., Knoepfler, P.S., Xie, S., Sherr, C.J., Eisenman, R.N., and Roussel, M.F. (2006). N-Myc and the cyclin-dependent kinase inhibitors p18Ink4c and p27Kip1 coordinately regulate cerebellar development. Proc. Natl. Acad. Sci. USA *103*, 11579–11583. https://doi.org/10.1073/pnas.0604727103.

15. Mirzamohammadi, F., Kozlova, A., Papaioannou, G., Paltrinieri, E., Ayturk, U.M., and Kobayashi, T. (2018). Distinct molecular pathways mediate Mycn and Myc-regulated miR-17-92 microRNA action in Feingold syndrome mouse models. Nat. Commun. *9*, 1352. https://doi.org/10.1038/s41467-018-03788-7.

16. Kato, K., Miya, F., Hamada, N., Negishi, Y., Narumi-Kishimoto, Y., Ozawa, H., Ito, H., Hori, I., Hattori, A., Okamoto, N., et al. (2019). MYCN *de novo* gain-of-function mutation in a patient with a novel megalencephaly syndrome. J. Med. Genet. *56*, 388–395. https://doi.org/10.1136/jmedgenet-2018-105487.

17. Frattini, V., Trifonov, V., Chan, J.M., Castano, A., Lia, M., Abate, F., Keir, S.T., Ji, A.X., Zoppoli, P., Niola, F., et al. (2013). The integrated landscape of driver genomic alterations in glioblastoma. Nat. Genet. *45*, 1141–1149. https://doi.org/10.1038/ng.2734.

18. Mirkovic, J., Sholl, L.M., Garcia, E., Lindeman, N., MacConaill, L., Hirsch, M., Dal Cin, P., Gorman, M., Barletta, J.A., Nucci, M.R., et al. (2015). Targeted genomic profiling reveals recurrent KRAS mutations and gain of chromosome 1q in mesonephric carcinomas of the female genital tract. Mod. Pathol. *28*, 1504–1514. https://doi.org/10.1038/modpathol.2015.103.

19. Sears, R., Nuckolls, F., Haura, E., Taya, Y., Tamai, K., and Nevins, J.R. (2000). Multiple Ras-dependent phosphorylation pathways regulate Myc protein stability. Genes Dev. *14*, 2501–2514. https://doi.org/10.1101/gad.836800.

20. Sjostrom, S.K., Finn, G., Hahn, W.C., Rowitch, D.H., and Kenney, A.M. (2005). The Cdk1 complex plays a prime role in regulating N-myc phosphorylation and turnover in neural precursors. Dev. Cell *9*, 327–338. https://doi.org/10.1016/j.devcel.2005.07.014.

21. Weiss, W.A., Aldape, K., Mohapatra, G., Feuerstein, B.G., and Bishop, J.M. (1997). Targeted expression of MYCN causes neuroblastoma in transgenic mice. EMBO J. *16*, 2985–2995. https://doi.org/10.1093/emboj/16.11.2985.

22. Otsuji, S., Nishio, Y., Tsujita, M., Rio, M., Huber, C., Antón-Plá-garo, C., Mizuno, S., Kawano, Y., Miyatake, S., Simon, M., et al. (2023). Clinical diversity and molecular mechanism of VPS35L-associated Ritscher-Schinzel syndrome. J. Med. Genet. *60*, 359–367. https://doi.org/10.1136/jmg-2022-108602.

23. Suzuki, H., Nozaki, M., Yoshihashi, H., Imagawa, K., Kajikawa, D., Yamada, M., Yamaguchi, Y., Morisada, N., Eguchi, M., Oha-shi, S., et al. (2022). Genome Analysis in Sick Neonates and In-fants: High-yield Phenotypes and Contribution of Small Copy Number Variations. J. Pediatr. *244*, 38–48.e1. https://doi.org/10.1016/j.jpeds.2022.01.033.

24. Hamada, N., Iwamoto, I., Tabata, H., and Nagata, K.I. (2017). MUNC18-1 gene abnormalities are involved in neurodevelop-mental disorders through defective cortical architecture dur-ing brain development. Acta Neuropathol. Commun. *5*, 92. https://doi.org/10.1186/s40478-017-0498-5.

25. Kanda, Y. (2013). Investigation of the freely available easy-to-use software 'EZR' for medical statistics. Bone Marrow Trans-plant. *48*, 452–458. https://doi.org/10.1038/bmt.2012.244.

26. Sobreira, N., Schiettecatte, F., Valle, D., and Hamosh, A. (2015). GeneMatcher: a matching tool for connecting investi-gators with an interest in the same gene. Hum. Mutat. *36*, 928–930. https://doi.org/10.1002/humu.22844.

27. Karczewski, K.J., Francioli, L.C., Tiao, G., Cummings, B.B., Al-földi, J., Wang, Q., Collins, R.L., Laricchia, K.M., Ganna, A., Birnbaum, D.P., et al. (2020). The mutational constraint spec-trum quantified from variation in 141,456 humans. Nature *581*, 434–443. https://doi.org/10.1038/s41586-020-2308-7.

28. Tate, J.G., Bamford, S., Jubb, H.C., Sondka, Z., Beare, D.M., Bindal, N., Boutselakis, H., Cole, C.G., Creatore, C., Dawson, E., et al. (2019). COSMIC: the Catalogue Of Somatic Muta-tions In Cancer. Nucleic Acids Res. *47*, D941–D947. https://doi.org/10.1093/nar/gky1015.

29. Kircher, M., Witten, D.M., Jain, P., O'Roak, B.J., Cooper, G.M., and Shendure, J. (2014). A general framework for estimating the relative pathogenicity of human genetic variants. Nat. Genet. *46*, 310–315. https://doi.org/10.1038/ng.2892.

30. Yada, M., Hatakeyama, S., Kamura, T., Nishiyama, M., Tsune-matsu, R., Imaki, H., Ishida, N., Okumura, F., Nakayama, K., and Nakayama, K.I. (2004). Phosphorylation-dependent degra-dation of c-Myc is mediated by the F-box protein Fbw7. EMBO J. *23*, 2116–2125. https://doi.org/10.1038/sj.emboj.7600217.

31. Kenney, A.M., Cole, M.D., and Rowitch, D.H. (2003). *Nmyc*u-pregulation by sonic hedgehog signaling promotes prolifera-tion in developing cerebellar granule neuron precursors. Development *130*, 15–28. https://doi.org/10.1242/dev.00182.

32. Corrales, J.D., Rocco, G.L., Blaess, S., Guo, Q., and Joyner, A.L. (2004). Spatial pattern of sonic hedgehog signaling through *Gli* genes during cerebellum development. Development *131*, 5581–5590. https://doi.org/10.1242/dev.01438.

33. Izumi, H., Kaneko, Y., and Nakagawara, A. (2020). The Role of MYCN in Symmetric vs. Asymmetric Cell Division of Human Neuroblastoma Cells. Front. Oncol. *10*, 570815. https://doi.org/10.3389/fonc.2020.570815.

34. Matsuzaki, F., and Shitamukai, A. (2015). Cell Division Modes and Cleavage Planes of Neural Progenitors during Mammalian Cortical Development. Cold Spring Harb. Perspect. Biol. *7*, a015719. https://doi.org/10.1101/cshperspect.a015719.

35. Huttner, W.B., and Kosodo, Y. (2005). Symmetric versus asym-metric cell division during neurogenesis in the developing vertebrate central nervous system. Curr. Opin. Cell Biol. *17*, 648–657. https://doi.org/10.1016/j.ceb.2005.10.005.

36. Götz, M., and Huttner, W.B. (2005). The cell biology of neuro-genesis. Nat. Rev. Mol. Cell Biol. *6*, 777–788. https://doi.org/10.1038/nrm1739.

37. Mitsuhashi, T., and Takahashi, T. (2009). Genetic regulation of proliferation/differentiation characteristics of neural progeni-tor cells in the developing neocortex. Brain Dev. *31*, 553–557. https://doi.org/10.1016/j.braindev.2009.05.002.

38. Riddle, R.D., Johnson, R.L., Laufer, E., and Tabin, C. (1993). Sonic hedgehog mediates the polarizing activity of the ZPA. Cell *75*, 1401–1416. https://doi.org/10.1016/0092-8674(93)90626-2.

39. Ahn, S., and Joyner, A.L. (2004). Dynamic changes in the response of cells to positive hedgehog signaling during mouse limb patterning. Cell *118*, 505–516. https://doi.org/10.1016/j.cell.2004.07.023.

40. Harfe, B.D., Scherz, P.J., Nissim, S., Tian, H., McMahon, A.P., and Tabin, C.J. (2004). Evidence for an expansion-based tempo-ral Shh gradient in specifying vertebrate digit identities. Cell *118*, 517–528. https://doi.org/10.1016/j.cell.2004.07.024.

41. Francis-West, P., and Hill, R. (2008). Uncoupling the role of sonic hedgehog in limb development: growth and specifica-tion. Sci. Signal. *1*, pe34. https://doi.org/10.1126/scisignal.126pe34.

42. Nakajima, T., Iguchi, T., and Sato, T. (2012). Hedgehog signaling plays roles in epithelial cell proliferation in neonatal mouse uterus and vagina. Cell Tissue Res. *348*, 239–247. https://doi.org/10.1007/s00441-012-1350-7.

43. Hsieh, C.L., Jerman, S.J., and Sun, Z. (2022). Non-cell-autono-mous activation of hedgehog signaling contributes to disease progression in a mouse model of renal cystic ciliopathy. Hum. Mol. Genet. *31*, 4228–4240. https://doi.org/10.1093/hmg/ddac175.

44. Silva, L.M., Jacobs, D.T., Allard, B.A., Fields, T.A., Sharma, M., Wallace, D.P., and Tran, P.V. (2018). Inhibition of Hedgehog signaling suppresses proliferation and microcyst formation of human Autosomal Dominant Polycystic Kidney Disease cells. Sci. Rep. *8*, 4985. https://doi.org/10.1038/s41598-018-23341-2.

45. Chen, J., and Guan, Z. (2022). Function of Oncogene Mycn in Adult Neurogenesis and Oligodendrogenesis. Mol. Neurobiol. *59*, 77–92. https://doi.org/10.1007/s12035-021-02584-7.

46. Hossain, M.S., Ozaki, T., Wang, H., Nakagawa, A., Takenobu, H., Ohira, M., Kamijo, T., and Nakagawara, A. (2008). N-MYC promotes cell proliferation through a direct transacti-vation of neuronal leucine-rich repeat protein-1 (NLRR1) gene in neuroblastoma. Oncogene *27*, 6075–6082. https://doi.org/10.1038/onc.2008.200.

47. Ribeiro, D., Ellwanger, K., Glagow, D., Theofilopoulos, S., Corsini, N.S., Martin-Villalba, A., Niehrs, C., and Arenas, E. (2011). Dkk1 regulates ventral midbrain dopaminergic differ-entiation and morphogenesis. PloS One *6*, e15786. https://doi.org/10.1371/journal.pone.0015786.

48. Westermann, F., Muth, D., Benner, A., Bauer, T., Henrich, K.-O., Oberthuer, A., Brors, B., Beissbarth, T., Vandesompele, J., Pat-tyn, F., et al. (2008). Distinct transcriptional MYCN/c-MYC ac-tivities are associated with spontaneous regression or malignant progression in neuroblastomas. Genome Biol. *9*, R150. https://doi.org/10.1186/gb-2008-9-10-r150.

Supplemental information

Gain-of-function *MYCN* causes

a megalencephaly-polydactyly syndrome manifesting

mirror phenotypes of Feingold syndrome

Yosuke Nishio, Kohji Kato, Frederic Tran Mau-Them, Hiroshi Futagawa, Chloé Quélin, Saori Masuda, Antonio Vitobello, Shiomi Otsuji, Hossam H. Shawki, Hisashi Oishi, Christel Thauvin-Robinet, Toshiki Takenouchi, Kenjiro Kosaki, Yoshiyuki Takahashi, and Shinji Saitoh
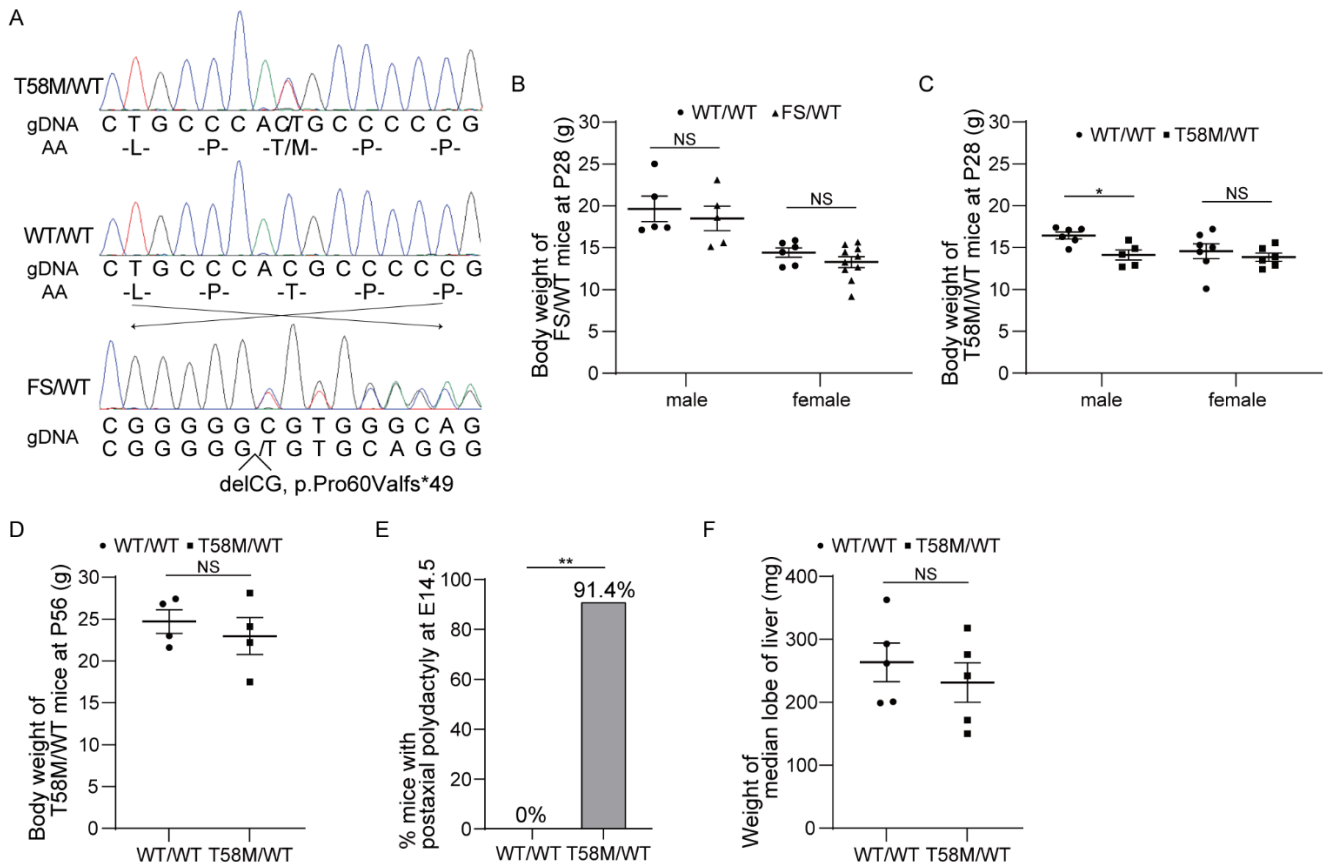
Figure S1. Genotyping and basic characterization of *Mycn* gain-of-function (T58M/WT) and haplo-insufficient mice (FS/WT).

(**A**) Sanger genotype sequencing for FS/WT, WT/WT and T58M/WT mice. (**B**) Body weight comparison between FS/WT and WT/WT at P28. Body weight of male and female FS/WT mice showed no significant difference compared with littermate WT/WT controls (WT/WT, n = 5; FS/WT, n = 5 for males; WT/WT, n = 6; FS/WT, n = 10 for females). (**C**) Body weight comparison between T58M/WT and WT/WT at P28. The body weight of male T58M/WT mice was slightly lower compared with littermate WT/WT controls, while that of the female mice showed no difference (WT/WT, n = 6; T58M/WT, n = 5 for males; WT/WT, n = 7; T58M/WT, n = 6 for females). (**D**) Body weight of male T58M/WT mice at P56. The body weight of male T58M/WT mice at P56 showed no difference compared with littermate WT/WT controls (WT/WT, n = 4; T58M/WT, n = 4). (**E**) Proportion of mice showing postaxial polydactyly at E14.5. In all, 91.4% of T58M/WT mice showed postaxial polydactyly at E14.5. (**F**) Weight of the median lobe of the liver showing no significant difference between T58M/WT and WT/WT mice. For bar graphs and scatter plots, means and SEM are shown; *$P < 0.05$, **$P < 0.01$. NS, not significant.

Table S1. List of antibodies and reagents.

Antibody/reagent	Clone	Manufacturer	#Product	Concentration/dosage
Western blot				
MYCN	B8.4.B	Santa Cruz Biotechnology	sc-53993	1:1000
c-Myc (phospho T58)	Polyclonal	abcam	ab28842	1:1000
Myc-tag	Polyclonal	MBL Life science	562	1:1000
GAPDH	D16H11	Cell Signaling Technology	5174	1:10000
Immunohistochemistry				
Neun	D3S3I	Cell Signaling Technology	12943	1:400
Neun	A60	Sigma-Aldrich	MAB377	1:400
Tbr2	BLR104H	abcam	ab275960	1:400
Pax6	Polyclonal	BioLegend	PRB-278P	1:400
Ki67	SP6	abcam	ab16667	1:400
Tbr1	EPR8138(2)	abcam	ab183032	1:400
Satb2	SATBA4B10	Santa Cruz Biotechnology	sc-81376	1:400
MVH	Polyclonal	abcam	ab13840	1:500
Rat IgG (H+L) Alexa 555	Polyclonal	Invitrogen	A-21434	1:750
Mouse IgG1 Alexa 555	Polyclonal	Invitrogen	A-21127	1:750
Mouse IgG1 Alexa 647	Polyclonal	Invitrogen	A-21240	1:750
Mouse IgG2a Alexa 488	Polyclonal	Invitrogen	A-21131	1:750
Mouse IgG2a Alexa 555	Polyclonal	Invitrogen	A-21137	1:750
Mouse IgG2b Alexa 488	Polyclonal	Invitrogen	A-21141	1:750
EdU (5-ethynil-2'-deoxyuridine)	–	abcam	ab146186	50 mg/kg/pregnant mouse
Azide-fluor 488	–	Sigma-Aldrich	760765	2 µM (final conc.)
DAPI	–	Roche	10236276001	1 µg/mL (final conc.)